



MIT Open Access Articles

Accurate measurement of in-plane thermal conductivity of layered materials without metal film transducer using frequency domain thermorefectance

The MIT Faculty has made this article openly available. **Please share** how this access benefits you. Your story matters.

Citation	Qian, Xin et al. "Accurate measurement of in-plane thermal conductivity of layered materials without metal film transducer using frequency domain thermorefectance." Review of Scientific Instruments 91, 6 (June 2020): 064903
As Published	http://dx.doi.org/10.1063/5.0003770
Publisher	AIP Publishing
Version	Author's final manuscript
Citable link	https://hdl.handle.net/1721.1/125778
Terms of Use	Creative Commons Attribution-Noncommercial-Share Alike
Detailed Terms	http://creativecommons.org/licenses/by-nc-sa/4.0/

Accurate Measurement of In-plane Thermal Conductivity of Layered Materials without Metal Film Transducer using Frequency Domain Thermoreflectance

Xin Qian, Zhiwei Ding, Jungwoo Shin, Aaron J. Schmidt, and Gang Chen*

Department of Mechanical Engineering,

Massachusetts Institute of Technology, Cambridge, MA 02139, USA

Corresponding Email: gchen2@mit.edu**Abstract**

Measuring anisotropic thermal conductivity has always been a challenging task in thermal metrology. Although recent developments of pump-probe thermoreflectance techniques such as variable spot sizes, offset pump-probe beams and elliptical beams have enabled the measurement of anisotropic thermal conductivity, a metal film transducer for the absorption of the modulated pump laser beam and the detection of the thermoreflectance signal. However, the existence of the transducer would cause in-plane heat spreading, suppressing the measurement sensitivity to the in-plane thermal conductivity. In addition, the transducer film also adds complexity to data processing, since it requires careful calibration or fitting to determine extra parameters such as the film thickness and conductivity, and interface conductance between the transducer and the sample. In this work, we discussed the methodology for measuring in-plane thermal conductivity of layered semiconductors and semimetals without any transducer layer. We show that the removal of transducer results in the dominantly large sensitivity to in-plane thermal conductivity compared with other parameters, such as cross-plane thermal conductivity and the absorption depth of the laser beams. Transducerless frequency-domain thermoreflectance (FDTR) measurements are performed on three reference layered-materials, highly ordered pyrolytic graphite (HOPG), molybdenum disulfide (MoS_2) and bismuth selenide (Bi_2Se_3), and demonstrated using the analytical thermal model that the measured in-plane thermal conductivity

showed much-improved accuracy compared with conventional FDTR measurement with a transducer.

I. Introduction

Anisotropic materials are commonly found in lots of applications such as thermoelectrics,^{1,2} power electronics³⁻⁵ and lithium-ion batteries.⁶⁻¹¹ Characterizing anisotropic thermal conductivity of these materials is not only of interest to scientific communities but also of fundamental importance to designing and advancing such technologies. In recent years, several pump-probe techniques based on either time-domain thermoreflectance (TDTR)^{12, 13} or frequency-domain thermoreflectance (FDTR)¹⁴⁻¹⁶ have been developed for measuring the anisotropic thermal conductivity of materials. For example, the in-plane thermal conductivity k_r and the cross-plane thermal conductivity k_z of transversely isotropic materials can be separately measured by tuning the laser spot size and/or the modulation frequency of the lasers.^{5, 17-19} Further, the beam-offset approach developed by Feser et al.²⁰ and the elliptical beam approach by Jiang et al.²¹ and Li et al.²² were shown capable of measuring the in-plane anisotropic thermal conductivity using TDTR. All these techniques require metal transducer films for the absorption of the pump beam and the detection of thermoreflectance to serve as the heater and the thermometer. The existence of metal films, however, would cause in-plane heat spreading that suppresses the sensitivity to the in-plane thermal conductivity, especially for transducers with high thermal conductivity such as aluminum and gold.^{21, 23} Although using thinner transducers with low thermal conductivity such as NbV helps to increase the measurement sensitivity,²⁴ accurate measurement of k_r remains challenging for materials with low in-plane thermal conductivity $k_r < 5$ W/mK.²³

This is the author's peer reviewed, accepted manuscript. However, the online version of record will be different from this version once it has been copyedited and typeset.
PLEASE CITE THIS ARTICLE AS DOI:10.1063/1.50003770

In this paper, we show that the in-plane thermal conductivity of layered semiconductors or semimetals can be accurately determined without using any metal transducers. Similar to the method by Yang et. al.,²⁵ we consider the optical absorption of a semi-infinite non-transparent sample by solving a thermal model with nonhomogeneous source terms for volumetric heating. However, full thermal conductivity tensor is included in the thermal model such that it is applicable to any crystalline symmetry. Three layered materials are measured using both conventional FDTR and beam-offset technique in this work, including HOPG, MoS₂ and Bi₂Se₃ with in-plane thermal conductivity ranging from a few W/mK to ~2000 W/mK. Measurement results using both techniques showed excellent consistency and agree well with the literature values.

II. Thermal Model with Light Absorption and Full Thermal Conductivity Tensor

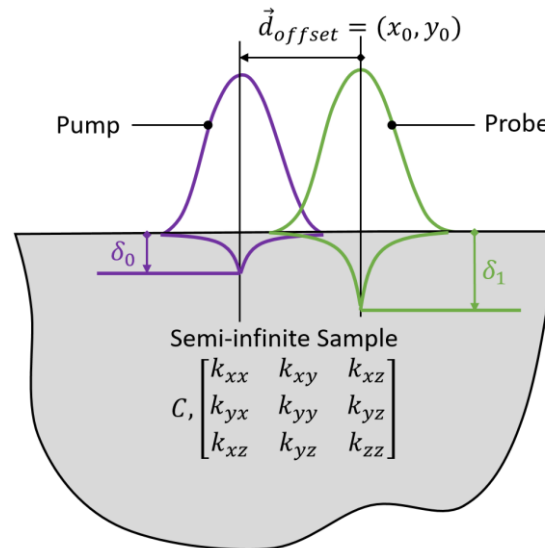


Figure 1. Schematic of a semi-infinite sample during a pump-probe measurement with offset pump and probe beam. The pump and probe lasers have $1/e$ absorption depths of δ_0 and δ_1 , respectively. The thermal properties of the semi-infinite sample include volumetric heat capacity C and the thermal conductivity tensor k_{ij} where $i, j = (x, y, z)$.

Figure 1 shows a measurement configuration with offset pump and probe beams on a semi-infinite solid. No crystalline symmetry is assumed here and the model includes the full thermal conductivity tensor k_{ij} . Using such configuration, the solution in principle can be used for any type of anisotropy, and for either conventional FDTR measurement with overlapping pump and probe, or the beam-offset FDTR measurements. To model the optical absorption of the pump laser, an exponentially decaying source terms is added to the heat equation:²⁶

$$C \frac{\partial T}{\partial t} = k_{ij} \frac{\partial^2 T}{\partial x_i \partial x_j} + \frac{1}{\delta_0} P(x, y, t) \cdot e^{-\frac{z}{\delta_0}} \quad (1)$$

where C is the volumetric heat capacity, k_{ij} is the thermal conductivity tensor element with $i, j = (x, y, z)$ denotes the Cartesian coordinates, which is symmetric $k_{ij} = k_{ji}$ due to the Onsager reciprocity and time-reversal symmetry.²⁷ $P(x, y, t)$ is the profile of the heat generation at the sample surface due to the pump laser. δ_0 is the absorption depth of the pump-laser. Instead of surface heat flux, the laser heating in transducerless configuration is modeled as a volumetric heat source with an exponential decaying profile. Such exponential form $\frac{1}{\delta_0} P(x, y, t) \cdot e^{-\frac{z}{\delta_0}}$ can be obtained by solving Maxwell's equation in an absorbing media,²⁸ which is valid as long as the characteristic length of δ_0 is much longer than the diffusion length of the photo-excited carriers.^{25, 29} Taking the Fourier transform to both in-plane coordinates x, y and the to time t such that $T(t, x, y, z) \rightarrow \theta(\omega, \xi, \eta, z)$, the heat equation is rewritten as:

$$i\omega C\theta = -(k_{xx}\xi^2 + k_{yy}\eta^2 + 2k_{xy}\xi\eta)\theta + k_{zz} \frac{d^2\theta}{dz^2} + 2i(k_{xz}\xi + k_{yz}\eta) \frac{d\theta}{dz} + \frac{1}{\delta_0} P(\xi, \eta, \omega) \cdot e^{-\frac{z}{\delta_0}} \quad (2)$$

Eq. (2) can be rearranged as an inhomogeneous ordinary differential equation:

$$\frac{d^2\theta}{dz^2} + \lambda_2 \frac{d\theta}{dz} - \lambda_1\theta + \frac{1}{k_{zz}\delta_0} P(\xi, \eta, \omega) \cdot e^{-\frac{z}{\delta_0}} = 0 \quad (3)$$

where

$$\lambda_1 = \frac{i\omega C}{k_{zz}} + \left(\frac{k_{xx}}{k_{zz}} \xi^2 + \frac{2k_{xy}}{k_{zz}} \xi\eta + \frac{k_{yy}}{k_{zz}} \eta^2 \right) \quad (4)$$

$$\lambda_2 = 2i \left(\frac{k_{xz}}{k_{zz}} \xi + \frac{k_{yz}}{k_{zz}} \eta \right) \quad (5)$$

With an adiabatic boundary condition $\left(\frac{d\theta}{dz}\right)_{z=0} = 0$ at the surface, the temperature response is solved as:

$$\theta(\omega, \xi, \eta, z) = \frac{P(\xi, \eta, \omega)}{k_{zz}\alpha(1 - \lambda_2\delta_0 - \lambda_1\delta_0^2)} \cdot \left(e^{-\alpha z} - \alpha\delta_0 e^{-\frac{z}{\delta_0}}\right) \quad (6)$$

where $\alpha = \frac{\lambda_2}{2} + \sqrt{\lambda_1^2 + \left(\frac{\lambda_2}{2}\right)^2}$. For a Gaussian pump beam, $P(\xi, \eta) = \frac{1}{2\pi} \exp\left[-\frac{w_0^2}{8}(\xi^2 + \eta^2)\right]$ where w_0 is the $1/e^2$ radius.

Different from conventional FDTR model using surface reflection when the sample is coated with transducer, calculating transducerless FDTR signal needs to consider bulk reflection of the probe beam, and the reflectance generated by θ depends on the depth. Therefore the FDTR signal $H(\omega)$ is calculated by integrating the temperature response over the z -dependent probe profile:²⁶

$$H(\omega, x_0, y_0) = \iint_{\mathbb{R}^2} \left[\int_0^\infty \theta(\omega, \xi, \eta, z) \cdot \frac{1}{\delta_1} S(\xi, \eta, x_0, y_0) \cdot e^{-\frac{z}{\delta_1}} dz \right] d\xi d\eta \quad (7)$$

where the integration range for (ξ, η) is the entire plane $\mathbb{R}^2 = (-\infty, \infty) \times (-\infty, \infty)$, δ_1 is the absorption depth of the probe beam as shown in Figure 1, and $S(\xi, \eta, x_0, y_0) = \frac{1}{2\pi} \exp\left(-\frac{w_1^2}{8}(\xi^2 + \eta^2)\right) \cdot \exp(i\xi x_0 + i\eta y_0)$ is the Fourier transform of the probe laser profile with $1/e^2$ radius of w_1 and offset coordinate (x_0, y_0) relative to the center of the pump beam. For the semi-infinite sample, the integration of z variable can be analytically obtained, and the final result for frequency-domain and offset-dependent FDTR signal $H(\omega, x_0, y_0)$ is calculated as:

$$H(\omega, x_0, y_0) = \frac{1}{4\pi^2} \iint_{\mathbb{R}^2} \mathcal{G}(\xi, \eta, \omega) \cdot e^{\left[-\frac{(w_0^2 + w_1^2)(\xi^2 + \eta^2)}{8}\right]} \cdot e^{(-i\xi x_0 - i\eta y_0)} d\xi d\eta \quad (8)$$

where the integration of ξ and η is over the entire plane $\mathbb{R}^2 = (-\infty, \infty) \times (-\infty, \infty)$, and the function \mathcal{G} is expressed as:

$$\mathcal{G}(\xi, \eta, \omega) = \frac{1}{k_{zz}\alpha(1 - \lambda_2\delta_0 - \lambda_1\delta_0^2)} \cdot \frac{\delta_0 + \delta_1 - \alpha\delta_0 - \alpha^2\delta_0\delta_1}{(1 + \alpha\delta_1)(\delta_0 + \delta_1)} \quad (9)$$

Eqs. (8) and (9) can be used for analyzing both the conventional frequency-sweep FDTR measurement by setting $x_0 = y_0 = 0$, and the beam-offset measurement with the fixed modulation frequency ω but varying the offset coordinates (x_0, y_0) .

Eqs (8-9) automatically recover the solution by Yang et al.²⁵ when using overlapped pump and probe beams and when the sample is transversely isotropic. In this case, the thermal conductivity tensor can be reduced to a diagonal tensor with diagonal elements $k_{xx} = k_{yy} = k_r$ and k_{zz} . Therefore, $\lambda_2 = 0$ and $\lambda_1 = q^2 = \frac{i\omega C + k_r \kappa^2}{k_{zz}}$, where q is the thermal wavenumber in cylindrical symmetry and $\kappa^2 = \xi^2 + \eta^2$ is identical to the Hankel transform variable. Eq. (8) can be further simplified as:

$$H(\omega) = \frac{1}{2\pi k_{zz}} \int_0^\infty \frac{\delta_0 + \delta_1 + q\delta_0\delta_1}{q(1 + q\delta_0)(1 + q\delta_1)(\delta_0 + \delta_1)} \cdot e^{\left(-\frac{w_0^2 + w_1^2}{8}\kappa^2\right)} \kappa d\kappa \quad (10)$$

which is identical to the result obtained by Yang et al.²⁵ It is clear that the FDTR signal can be determined by a single effective radius, which is written as the root-mean-squared (RMS) radius

$$w = \frac{w_0^2 + w_1^2}{2}.$$

To conclude this section, we briefly discuss the limitation of the model above. First, an exponentially decaying heat source term is only valid when the the charge carriers recombines fast and the diffusion lengths of these carriers are smaller than the light absorption depth δ_0 and δ_1 . One typical case when the model in this work fails is crystalline silicon with slow nonradiative recombination. Lifetime of photo-induced charge carriers in silicon could approach microsecond (μs) scale and the diffusion length is estimated to even approach $\sim 10^2 \mu\text{m}$.³⁰ As a result, the nonradiative recombination of electrons and holes generates heat in much larger region beyond the exponentially decaying light intensity profile. Indeed we found the derived model above would not be able to fit FDTR signal for crystalline silicon (See more discussion in the Appendix). Another limitation is that Eq. (7) neglected the spatial oscillating part of the reflectance change profile due to the interference incident and reflected probe light field,³¹ which is only valid when the probe light absorption depth δ_1 is much smaller than half of the wavelength in the media.²⁵ A typical example for this case is indeed GaAs with δ_1 comparable to the half-wavelength inside the media.³² Fortunately, this issue in GaAs can be partially solved by limiting the measurement at low modulation frequency $< 0.5 \text{ MHz}$ (See more discussion in the Appendix). Finally, local equilibrium is also assumed when deriving the model, namely, lattice and charge carriers being at the same temperature. This model, however, might no longer be valid if the electron-phonon interaction is weak and nonequilibrium transport is non-negligible.³³ Transducerless FDTR measurement of thermal conductivity in isotropic thin films on a transparent substrate has already been presented in ref ²⁵, and extending the solution to fully anisotropic thermal conductivity tensors will be done in the future. However, when the film thickness is much smaller than δ_0 such as few-layer 2D materials, relative small absorptance and reflectance of the sample might result in a very weak thermorefectance signal.

III. Measuring In-plane Thermal Conductivity without Transducer

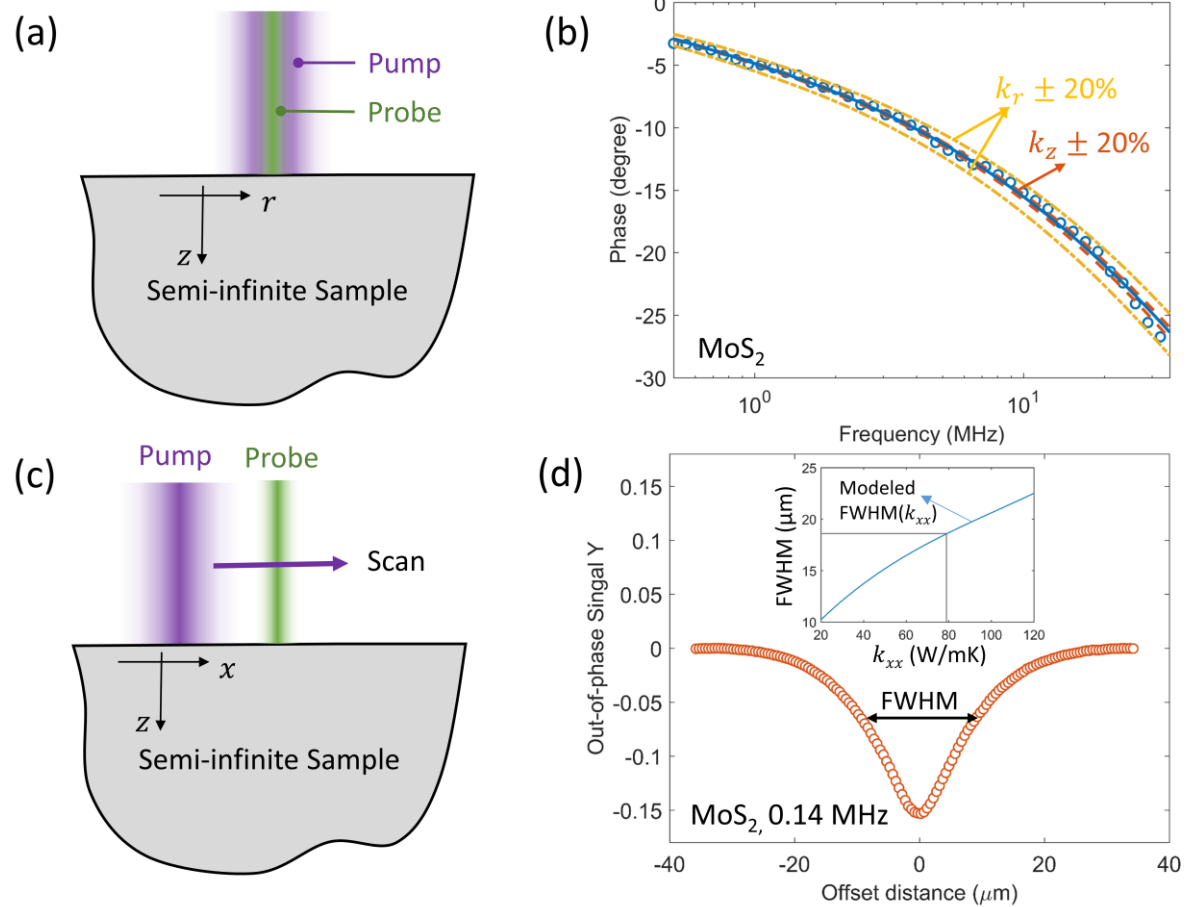


Figure 2. (a) Schematic of conventional frequency-sweep FDTR measurement with overlapped pump and probe beams. (b) Frequency-sweep FDTR signal obtained on the bare MoS_2 sample with the best fit value $k_r = 75$ W/mK, $k_z = 5.7$ W/mK. (c) Schematic of beam-offset measurement by varying the pump-offset distance with respect to the probe beam. (d) Out-of-phase beam-offset thermoreflectance signal obtained on the bare MoS_2 sample at the modulation frequency $f = 0.14$ MHz where FWHM of the out-of-phase signal is measured to obtain the in-plane thermal conductivity k_{xx} along the offset direction (x in the figure). Inset shows that k_{xx} is extracted as 79 W/mK from the simulated FWHM curve.

In this section, we discuss the measurement methodology of in-plane thermal conductivity using FDTR without transducer films. As shown in Figure 2, two measurement techniques are considered. The first technique is the conventional frequency-sweep FDTR measurement with overlapped pump and probe beams (Figure 2a), and the thermal conductivity is extracted by fitting the thermal phase ϕ as shown in Figure 2b. The other technique is the beam-offset technique as shown in Figure 2c where the out-of-phase thermorefectance signal Y (imaginary part of $H(\omega)$) at the fixed modulation frequency is measured as a function of the beam-offset distance as shown in Figure 2d. Then, by comparing the measured and the simulated full-width at half-maximum (FWHM), in-plane thermal conductivity along the offset direction can be extracted as shown in Figure 2d inset.²⁰

In the following discussions, we first show that without transducer films both the frequency-sweep measurement and the beam-offset measurement are dominantly sensitive to the in-plane thermal conductivity through sensitivity analysis in part A. In part B, error propagation in both frequency-sweep and beam-offset measurement will be discussed in detail. Finally, experimental results obtained with HOPG, MoS₂ and Bi₂Se₃ will be presented in part C.

A. Sensitivity Analysis

In general, the sensitivity of an observable y with respect to a certain property x is defined as:³⁴

$$S_x^y = \frac{\partial \ln y}{\partial \ln x} \quad (11)$$

The observable y can be either the thermal phase angle ϕ for the frequency-sweep measurement, or the FWHM of the out-of-phase signal in the case of the beam-offset measurement. x here can

be any properties or input parameters of interest, such as volumetric heat capacity, absorption depths, spot radius, just to name a few. Sensitivity essentially quantifies the propagation of relative change of x into the change of y . For example, a $S_x^y = 0.5$ indicates that 10% relative change in x would result in about 5% change of y . These sensitivities are also related to error propagation, which will be further discussed in part B.

Figure 3 shows the sensitivity of the thermal phase ϕ to the physical properties for the three reference layered samples, HOPG, MoS₂ and Bi₂Se₃ with and without transducers. Nominal parameters used to calculate the sensitivities are listed in Table I. Without the transducer, the sensitivity of thermal phase ϕ to in-plane thermal conductivity is systematically increased for all three samples, especially for HOPG and Bi₂Se₃. It is intuitive to understand that the sensitivity to the in-plane thermal conductivity is improved for all three samples, especially for Bi₂Se₃ with low in-plane thermal conductivity k_r , because of the absence of heat spreading caused by the transducer. Interestingly, the sensitivity to the absorption depths δ_0 and δ_1 are small for the three samples compared with k_r , especially at low modulation frequencies. This is can be attributed to the much larger thermal penetration dept than absorption depths. The thermal penetration depth is defined as $d_{pz} = \sqrt{k_{zz}/\pi C f}$, where k_{zz} is the cross-plane thermal conductivity, C is volumetric heat capacity and f is the modulation frequency. d_{pz} is on the order of a few μm when modulation frequency is lower than 1 MHz, much larger than the light absorption depths ~ 10 nm, therefore the through plane temperature profile is determined by d_{pz} instead of δ_0 or δ_1 . We calculated the absorption depths according to the extinction coefficient of the materials (also included in Table I) at the wavelengths of the pump (400 nm) and the probe (532 nm) beams. These absorption depths are treated as fixed parameters when fitting the signal. The low

sensitivity to δ_0 and δ_1 is also preferable, because this also means that uncertainty in these two parameters can hardly propagate to k_r .

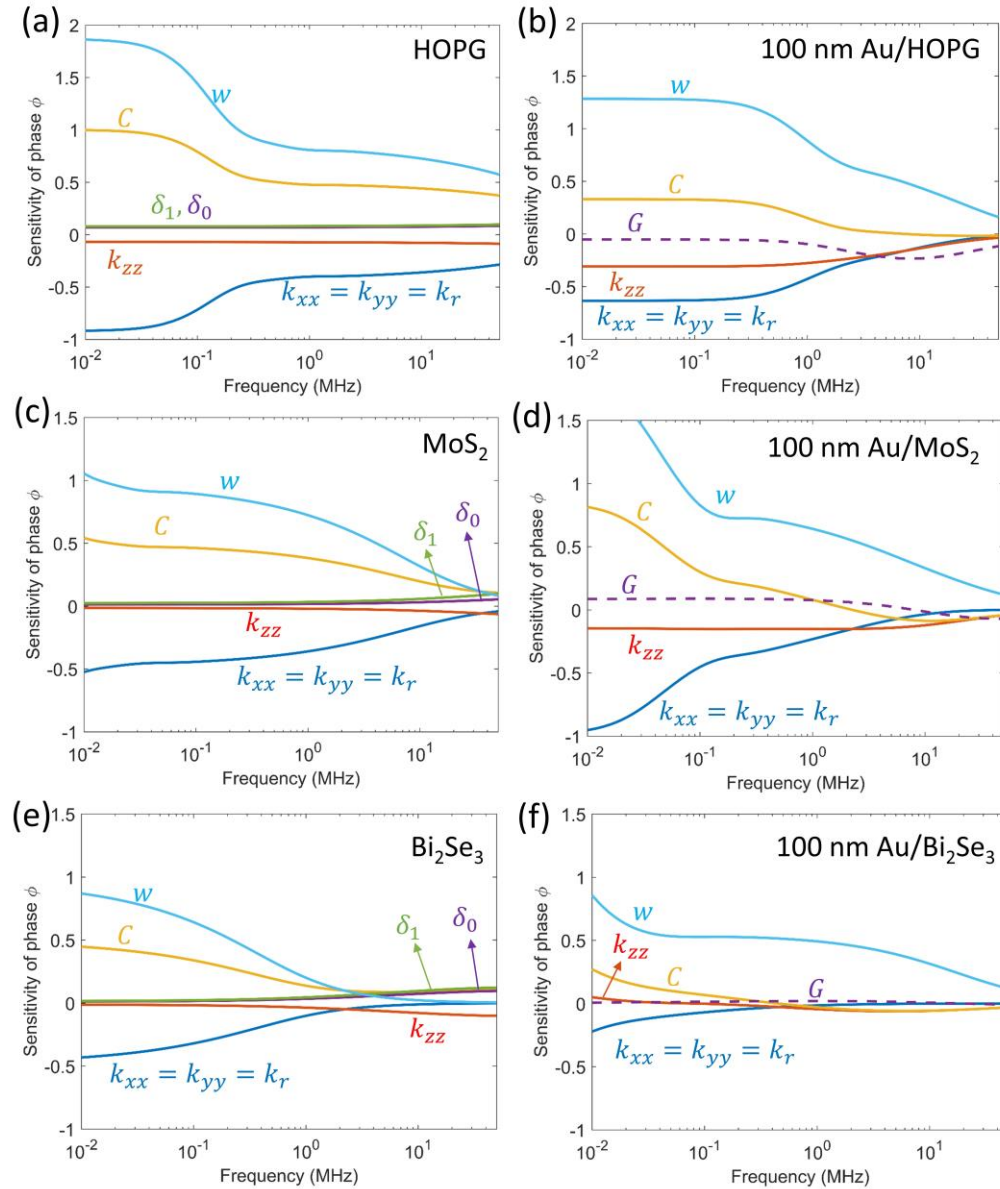


Figure 3. Calculated sensitivity of thermal phase ϕ to thermal properties of (a) bare HOPG sample, (b) 100 nm Au coated HOPG, (c) bare MoS₂ and (d) 100 nm Au coated MoS₂, (e) bare Bi₂Se₃ and (f) 100 nm Au coated Bi₂Se₃. Interface conductance is assumed as 40 MW/m²K for all samples, spot radius used for sensitivity analysis is $w = 2.8 \mu\text{m}$.

This is the author's peer reviewed, accepted manuscript. However, the online version of record will be different from this version once it has been copyedited and typeset.
PLEASE CITE THIS ARTICLE AS DOI:10.1063/1.50003770

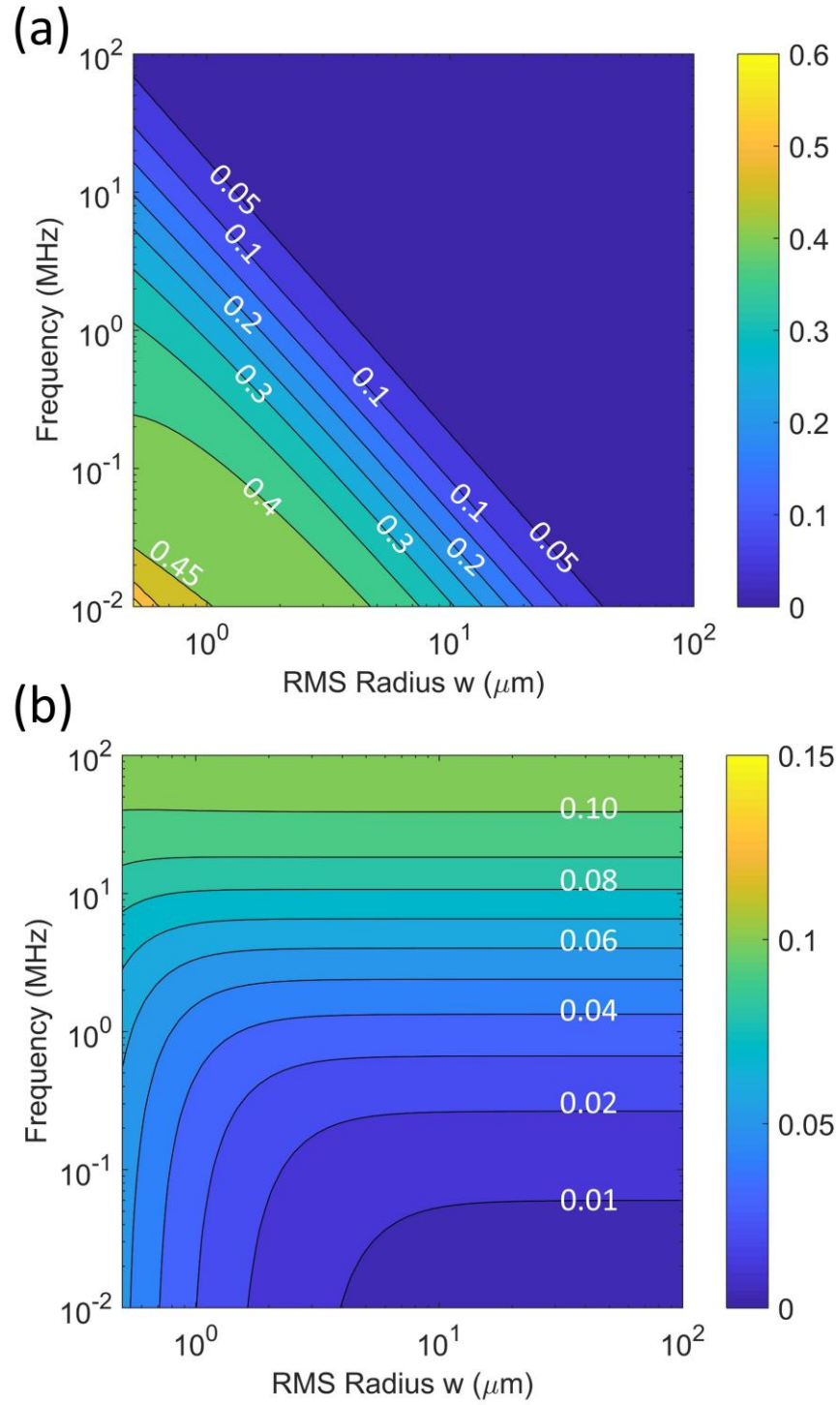


Figure 4. Contour of sensitivity to (a) in-plane thermal conductivity k_r and (b) cross-plane thermal conductivity k_z of Bi_2Se_3 .

Selecting appropriate spot radius and modulation frequency is especially important for measuring low in-plane thermal conductivity. In order to provide guidance to selecting spot radius, Figure 4a shows the contour of sensitivity to in-plane thermal conductivity for Bi_2Se_3 . When fixing a spot radius, high sensitivity to k_r is mostly in the low frequency range. To ensure a high sensitivity (>0.3) to in-plane thermal conductivity, the spot size is preferably below $10\ \mu\text{m}$, and the lower bound of frequency-sweep should be below $0.2\ \text{MHz}$. Since k_z is an extra unknown parameter, it would become difficult to determine k_r if the sensitivity to k_z is high. Figure 4b shows the sensitivity map to cross-plane thermal conductivity k_z . As long as the modulation frequency is below $40\ \text{MHz}$ (corresponding to penetration depth $d_{pz} \geq 63\ \text{nm}$), the sensitivity to k_z can be suppressed below 0.1 . Unlike conventional FDTR with transducers, it is hard to improve the sensitivity to cross-plane thermal conductivity in the experimental frequency range ($< 50\ \text{MHz}$ for our implementation) of transducerless FDTR measurements.

While the above analysis showed that conducting frequency-sweep measurement without any transducers is highly promising to obtain k_r for materials with isotropic in-plane thermal conductivity, it is still desirable to examine the sensitivity of beam-offset measurement especially for materials without in-plane symmetry, which solely measures the thermal conductivity along the offset direction. Figure 5 summarizes the sensitivity of FWHM of the out-of-phase signal for bare samples without transducers and samples coated with 100-nm Au transducer films. It is clear that the sensitivity of the in-plane thermal conductivity k_{xx} along the offset direction x and the heat capacity C are almost mirror image of each other, indicating that the beam-offset measurement essentially measures the in-plane diffusivity k_{xx}/C ,²⁰ therefore, C cannot be independently determined by beam-offset measurement. Other than k_{xx} and C the RMS spot radius w is also one of the most sensitive properties, which is indeed the major source

of uncertainty in beam-offset measurements.²⁰ In this work, we directly determine the spot radius w by fitting in-phase thermorefectance signal of the beam-offset measurement on MoS₂ and Bi₂Se₃ where the in-phase signal at a high modulation frequency of 40 MHz is fitted with a Gaussian beam profile $\exp(-x_0^2/w^2)$, where w is the RMS spot radius.²⁰ Another major advantage of the beam-offset measurement is the negligible sensitivity to the cross-plane thermal conductivity k_{zz} , and the absorption depths δ_0 and δ_1 . Therefore once the heat capacity is known, the beam-offset measurement without transducer film can solely determine in-plane thermal conductivity.

Figure 5b, d and f shows the comparison for the beam-offset measurement on samples coated with 100-nm Au films. Although sensitivity to k_{xx} is only moderately improved for HOPG and MoS₂ with relatively high in-plane thermal conductivity, the beam-offset measurement on bare samples without transducers is much simpler. Transducerless measurements do not involve the transducer thickness d_{Au} and the interface conductance G , which needs to be independently measured and adds complexity to the model. Removal of the transducer is particularly beneficial for measuring low in-plane thermal conductivity materials such as Bi₂Se₃ as shown in Figure 5e. For both conventional and transducerless beam-offset measurements, the thermorefectance signal is dominantly sensitive to k_{xx} if the modulation frequency is below 0.05 MHz. However, the sensitivity to k_{xx} would be overwhelmed by additional properties such as transducer thickness for the conventional beam-offset measurement, even if the modulation frequency is as low as 0.01 MHz.

For transducerless beam-offset measurements, there is a trade-off between the amplitude of the out-of-phase signal and the sensitivity to in-plane thermal conductivity. While Figure 5a, c and e showed that the sensitivity to k_{xx} increases as the modulation frequency decreases, it is not

This is the author's peer reviewed, accepted manuscript. However, the online version of record will be different from this version once it has been copyedited and typeset.
PLEASE CITE THIS ARTICLE AS DOI:10.1063/1.50003770

always beneficial to perform beam-offset measurement at the lowest possible frequency. However, the amplitude of out-of-phase signal also decreases with lower modulation frequency. For HOPG and MoS₂ with higher in-plane thermal conductivity, the out-of-phase signal would be at least one-order-magnitude smaller than the in-phase signal at low modulation frequency ~ 0.01 MHz. As a result, the measured FWHM would be easily affected by $1/f$ noise or slight shift of the pump-phase. Therefore, the in-plane thermal conductivity of MoS₂ and HOPG is measured at 0.14 MHz to ensure the accurate detection of the out-of-phase signal. For Bi₂Se₃ with much low in-plane thermal conductivity, however, we choose the lowest modulation frequency for beam-offset measurement to ensure the high sensitivity to k_{xx} . The sample measurement discussion will be continued in part C.

This is the author's peer reviewed, accepted manuscript. However, the online version of record will be different from this version once it has been copyedited and typeset.
PLEASE CITE THIS ARTICLE AS DOI:10.1063/1.50003770

Table I. Input parameters and uncertainties (σ) for the sensitivity analysis. Uncertainties of k_{xx} or k_r and k_{zz} are to be determined by error propagation, which will be discussed later. The absorption depths are estimated as $\delta = \frac{\lambda}{4\pi\kappa}$ where κ is the extinction coefficient and λ is the wavelength. References for extinction coefficients are provided in the references.

	k_{xx} or k_r	k_{zz}	C	δ_0	δ_1	w
Units	W/mK	W/mK	MJ/m ³ K	nm	nm	μm
HOPG	1900 ¹⁹	6.1 ¹⁷	1.62 ³⁵	17 ³⁶	18 ³⁶	2.8
MoS ₂	80.0 ¹⁹	4.75 ¹⁹	1.91 ³⁷	11 ³⁸	14 ³⁸	2.8
Bi ₂ Se ₃	3.1 ³⁹	0.7 ⁴⁰	1.4 ⁴⁰	17 ⁴¹	19 ⁴¹	2.8
Uncertainty	NA	NA	5%	20%	20%	5%

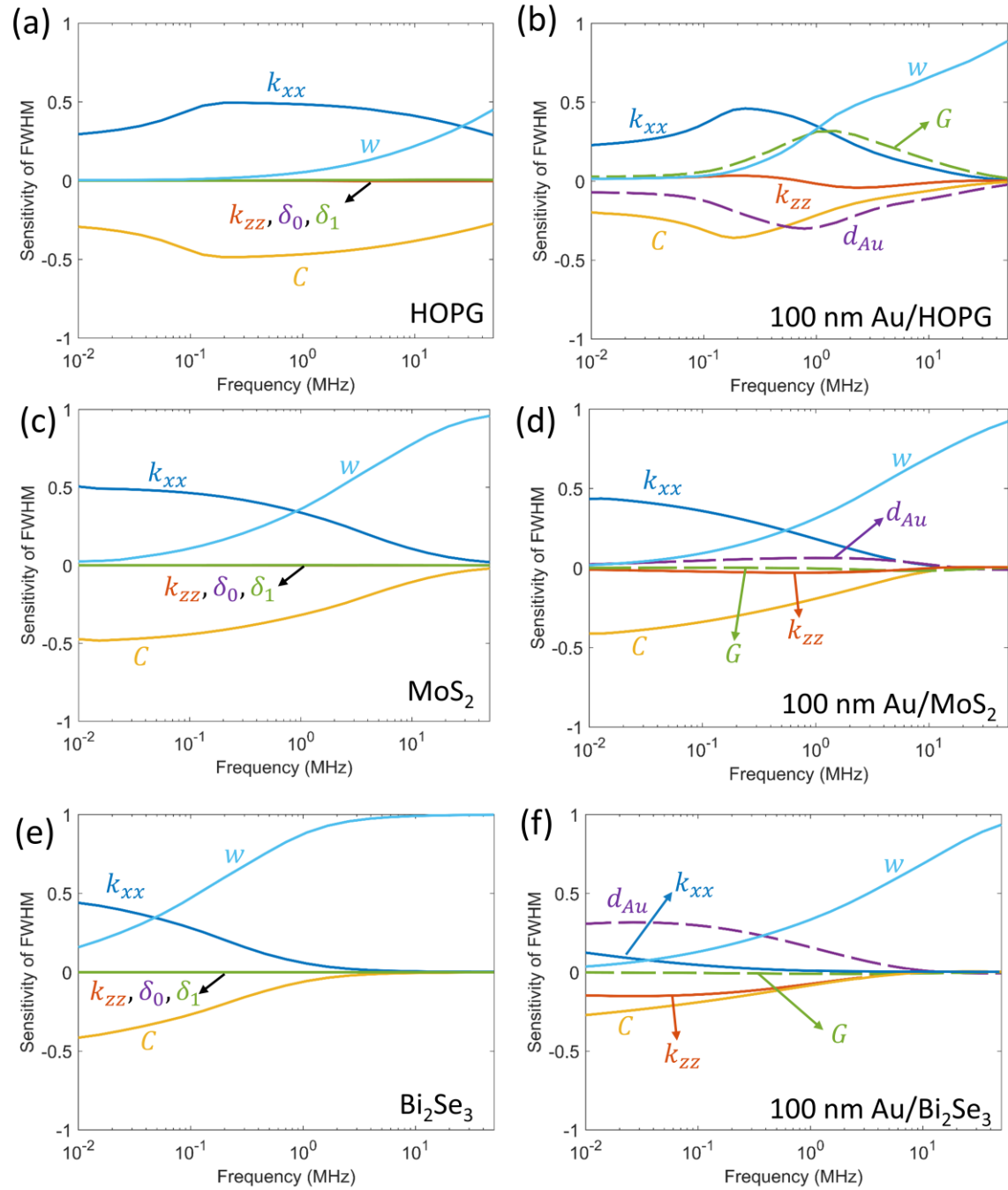


Figure 5. Calculated sensitivity of FWHM of the out-of-phase signal to thermal properties of (a) bare HOPG sample, (b) 100 nm Au coated HOPG, (c) bare MoS₂ and (d) 100 nm Au coated MoS₂, (e) bare Bi₂Se₃ and (f) 100 nm Au coated Bi₂Se₃. Interface conductance is assumed as 40 MW/m²K for all samples, spot radius used for sensitivity analysis is $w = 2.8 \mu\text{m}$.

B. Uncertainty Analysis

After the sensitivities are calculated, we now discuss the propagation of uncertainties. For the frequency-sweep measurement, a multivariate error propagation formula is derived by Yang et al.⁴² based on Jacobi matrices:

$$\text{var}[X_U] = (J_U^T J_U)^{-1} J_U^T (\text{var}[\phi] + J_C \text{var}[X_C] J_C^T) J_U (J_U^T J_U)^{-1} \quad (12)$$

where $\text{var}[X_U]$ denotes the covariance matrix of the unknown fitting variables such as k_r and k_{zz} , $\text{var}[X_C]$ is the covariance of the input variables such as the spot radius, absorption depths and so on. $\text{var}[\phi]$ is the noise level of phase in the measurement which contributes negligibly to the uncertainty. J_C and J_U are Jacobi matrices of the signal ϕ with respect to X_C or X_U , calculated as:

$$J_C = \begin{bmatrix} \frac{\partial \phi_1}{\partial x_{c1}} & \frac{\partial \phi_1}{\partial x_{c2}} & \cdots & \frac{\partial \phi_1}{\partial x_{cp}} \\ \frac{\partial \phi_2}{\partial x_{c1}} & \frac{\partial \phi_2}{\partial x_{c2}} & \cdots & \frac{\partial \phi_2}{\partial x_{cp}} \\ \vdots & \vdots & \ddots & \vdots \\ \frac{\partial \phi_N}{\partial x_{c1}} & \frac{\partial \phi_N}{\partial x_{c2}} & \cdots & \frac{\partial \phi_N}{\partial x_{cp}} \end{bmatrix}, \quad J_U = \begin{bmatrix} \frac{\partial \phi_1}{\partial x_{u1}} & \frac{\partial \phi_1}{\partial x_{u2}} & \cdots & \frac{\partial \phi_1}{\partial x_{uq}} \\ \frac{\partial \phi_2}{\partial x_{u1}} & \frac{\partial \phi_2}{\partial x_{u2}} & \cdots & \frac{\partial \phi_2}{\partial x_{uq}} \\ \vdots & \vdots & \ddots & \vdots \\ \frac{\partial \phi_N}{\partial x_{u1}} & \frac{\partial \phi_N}{\partial x_{u2}} & \cdots & \frac{\partial \phi_N}{\partial x_{uq}} \end{bmatrix} \quad (13)$$

where $\phi_i = \phi(\omega_i)$ is the phase measured at i -th modulation frequency out of N frequencies in total, x_{cj} and x_{uj} are the j -th parameter of the control variable vector X_C and fitting variable vector X_U . p and q are the total numbers of control variables and fitting variables. Finally, we visualize the confidence interval using:⁴³

$$(X_U - X_U^*)^T (\text{var}[X_U]) (X_U - X_U^*) = \chi_D^2 (p = 0.68) \quad (14)$$

where $\chi_D(p)$ is the quantile function, and D is the number of fitting variables, p is the confidence level taken as 0.68 in this work (i.e. each error bar is taken as one σ). For the frequency sweep measurement, $X_U = [k_r, k_{zz}]$ and $D = 2$, therefore typical confidence interval has an elliptical shape as shown in Figure 6a. Although uncertainty in k_{zz} is relatively large $\sim 37\%$, k_{zz} is weakly correlated with the in-plane thermal conductivity k_r , where k_r can be determined with uncertainty as low as 5% even k_{zz} remains unknown.

Uncertainty propagation in the beam-offset measurement is shown in Figure 6b, using MoS₂ as an example. Since the in-plane thermal conductivity k_{xx} along the beam-offset direction is determined by comparing the measured FWHM and the simulated function $\text{FWHM} = f(k_{xx}, X_C)$, there are indeed two sources of uncertainty. The first source of uncertainty in k_{xx} is contributed from the experimental uncertainty while the other source is the uncertainty in the model $f(k_{xx}, X_C)$ derived from the control parameters X_C . The experimental uncertainty of the measured FWHM ($\sim 0.2 \mu\text{m}$) can be easily derived from repeated measurements as shown in Figure 6b, which results in $\sim 2.4\%$ of uncertainty in k_{xx} . On the other hand, the relative uncertainty in the simulated FWHM is calculated as:²¹

$$\eta_{FWHM}^S = \sqrt{\sum_{x_c \in X_C} (S_{x_c}^{FWHM} \eta_{x_c})^2} \quad (15)$$

where η_x denotes the relative uncertainty of variable x . The uncertainty of simulated FWHM with the input control parameters with given uncertainties (Table 1) resulted in 5% uncertainty of k_{xx} , which is also plotted in Figure 6b. Finally, the overall uncertainty in k_{xx} is can be estimated using the root sum squares method as $\sqrt{2.4\%^2 + 5\%^2} = 5.5\%$.

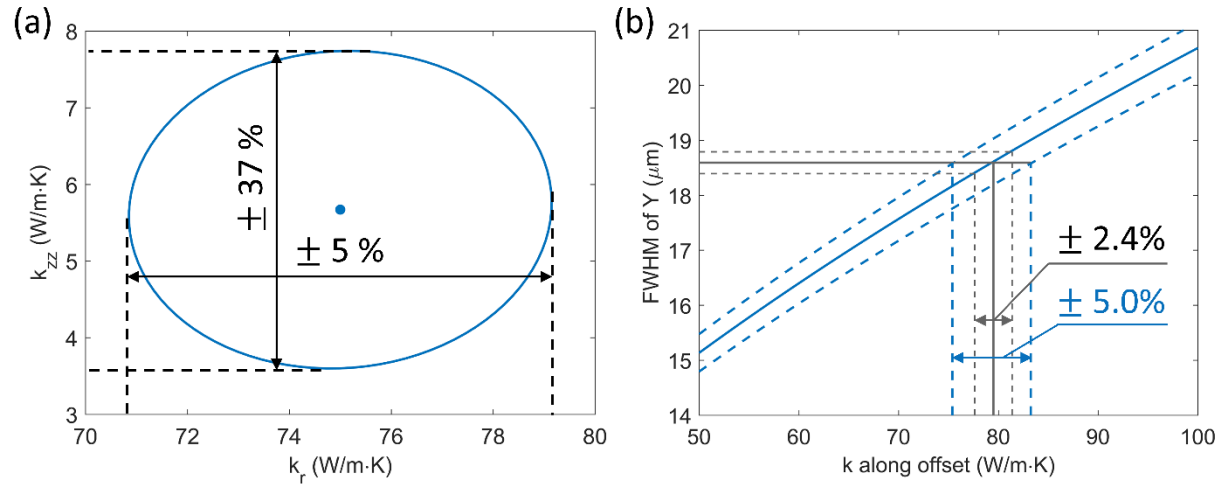


Figure 6. (a) Confidence interval for the frequency-sweep measurement on bare MoS₂. (b) Uncertainty propagation to the in-plane thermal conductivity of MoS₂ along the offset direction (k_{xx}). Gray dashed line indicates the experimental uncertainty contribution from the FWHM measured at $f = 0.14$ MHz, and the blue dashed line indicates the uncertainty contribution from the simulated FWHM as a function of k_{xx} with the uncertainty in control variables as shown in Table 1, including the spot radius and heat capacity.

C. Measurement Results

As a demonstration of measuring in-plane thermal conductivity without a transducer film, we conducted both frequency-sweep and beam-offset FDTR measurements on three layered anisotropic crystals (HOPG, MoS₂ and Bi₂Se₃), with in-plane thermal conductivity spans over three orders of magnitude. Our experimental system is similar to ref.⁴⁴, but employs a continuous-wave (cw) 400-nm pump laser and a 532-nm probe laser. Before conducting the measurements, we exfoliate the surface layers away using scotch tapes to expose the fresh

surfaces of the substrate. All samples measured in this work are in bulk form, purchased from 2D Semiconductors. Figure 7 summarizes the frequency-sweep thermoreflectance signal and the measured in-plane and cross-plane thermal conductivity with 68% confidence interval through the multi-parameter fitting. As shown in Figure 7a, except for Bi_2Se_3 above 2 MHz, the frequency-sweep signal is dominantly sensitive to the in-plane thermal conductivity k_r and is barely affected by the cross-plane thermal conductivity k_{zz} . As a result, uncertainty in k_{zz} is very large for all three samples, and increases as the in-plane thermal conductivity increases (30% for Bi_2Se_3 , 37 % for MoS_2 and 64% for HOPG). Nonetheless, such large uncertainty in k_{zz} would not compromise the measurement accuracy of in-plane thermal conductivities, as shown in Figure 7b. The relative uncertainties of the in-plane thermal conductivity are smaller than 15% for all three samples.

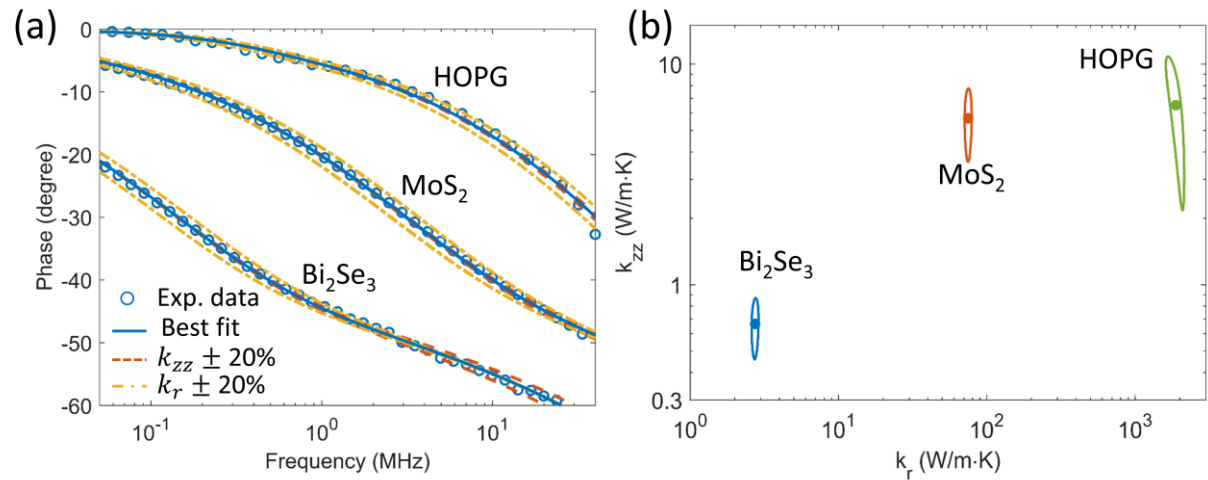


Figure 7. (a) Frequency-sweep FDTR signal and (b) measured anisotropic thermal conductivity with 68% confidence interval (solid curves) of the best fit (k_r, k_{zz}) (center dots) for Bi_2Se_3 , MoS_2 and HOPG without transducers.

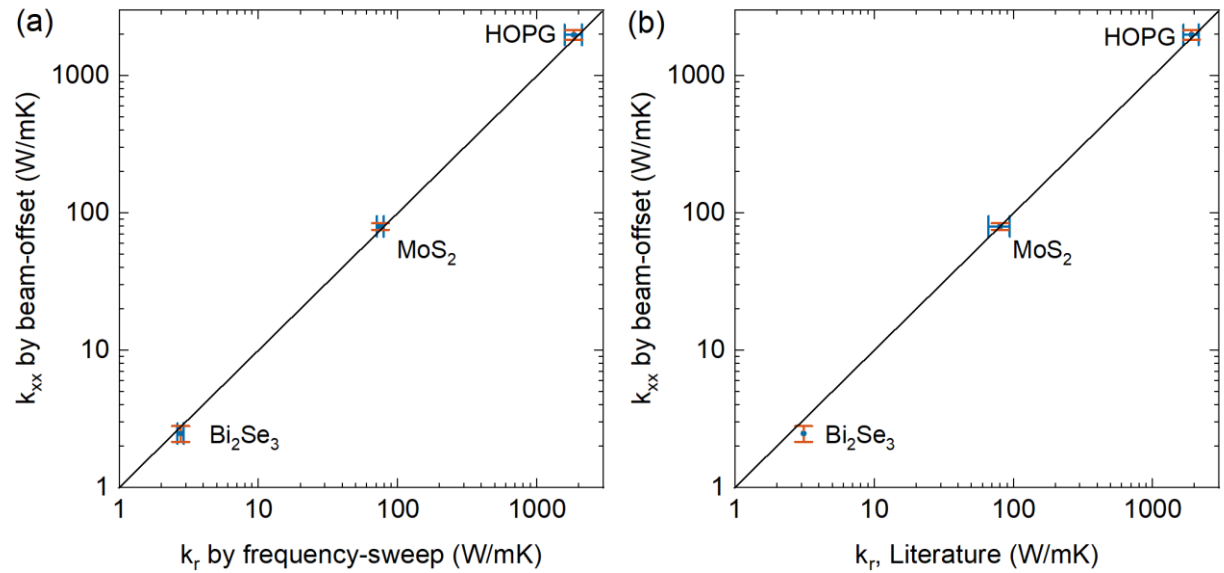


Figure 8. (a) Comparison of measured in-plane thermal conductivity obtained from beam-offset measurements (k_{xx}) and frequency sweep measurements (k_r) without the transducer. (b) In-plane thermal conductivity comparison between the transducerless beam-offset measurements and literature values. (refs HOPG,¹⁹ MoS₂,¹⁹ Bi₂Se₃³⁹)

Figure 8 summarizes the comparison between the in-plane thermal conductivity obtained by the beam-offset measurement and the frequency-sweep measurement (Figure 8a), and the literature values (Figure 8b). The excellent agreement has validated our measurement approach. All best-fit values and uncertainties are also tabulated in Table II. Although only three reference samples are measured in this work, we further envision that this method could be applied to other non-transparent materials as well. Figure 9a summarizes the predicted measurement error over a wide range of in-plane diffusivity, for both frequency-sweep and beam-offset measurements with or without transducers. In general, removal of the transducer always helps to improve the measurement accuracy except for the frequency-sweep on bare samples with in-plane thermal diffusivity (k_{xx}/C) higher than 1400 mm²/s. This is probably due to the fact of the overlapping

laser beam only samples the temperature profile within the spot radius, while the in-plane thermal penetration length could be a few orders of magnitude larger than the spot size. When in-plane thermal diffusivity is larger than $\sim 15 \text{ mm}^2/\text{s}$, it is advantageous to perform the beam-offset FDTR without the transducer. While for materials with low in-plane thermal diffusivity $< 15 \text{ mm}^2/\text{s}$, the frequency-sweep method could achieve high precision with relative uncertainty lower than 10%, as shown in Figure 9b. We also identified the optimal range for the conventional FDTR with transducers. For the beam-offset measurement with a 100-nm Au transducer film, the lower limit of in-plane thermal diffusivity is around $5 \text{ mm}^2/\text{s}$ to achieve less than 15% uncertainty in k_{xx} while the optimal range of in-plane diffusivity is limited between $1.6 \text{ mm}^2/\text{s}$ and $160 \text{ mm}^2/\text{s}$ for the frequency-sweep measurement with a 100-nm Au transducer film. Finally, steady state temperature rise would still be an important concern when performing transducerless measurements. Due to the small thermorefectance of the uncoated samples compared with metal transducers, large pump power might be required. For example, we found that the signal amplitude obtained on transducerless HOPG with 30 mW pump, 5 mW probe is only 1/30 of the signal of HOPG coated with 100 nm Au transducer using 5 mW pump, 1 mW probe. Steady state temperature rise might also be important for highly absorptive samples with low thermal conductivity. For example, the steady state temperature rise of Bi_2Se_3 is still estimated¹² to be relatively large $\sim 20 \text{ K}$ even when the laser power is suppressed to 0.2 mW with a RMS spot radius of $2.8 \text{ }\mu\text{m}$, which is close to the minimum operating power of the laser implemented in this work. In this work, we estimate the maximum temperature rise for all measurements using $\Delta T = P/(2w\sqrt{\pi k_r k_z})$,¹² where P is the total laser power, $w = 2.8 \text{ }\mu\text{m}$ is the laser spot radius, k_r and k_z are in-plane and through plane thermal conductivity respectively. Laser power is selected to ensure steady state temperature rise below 30 K. Another possible solution to

suppress steady-state temperature rise is to employ less focused laser spots, since steady state temperature rise scales w^{-1} with the RMS spot radius according to the semi-infinite body solution of heat conduction.¹²

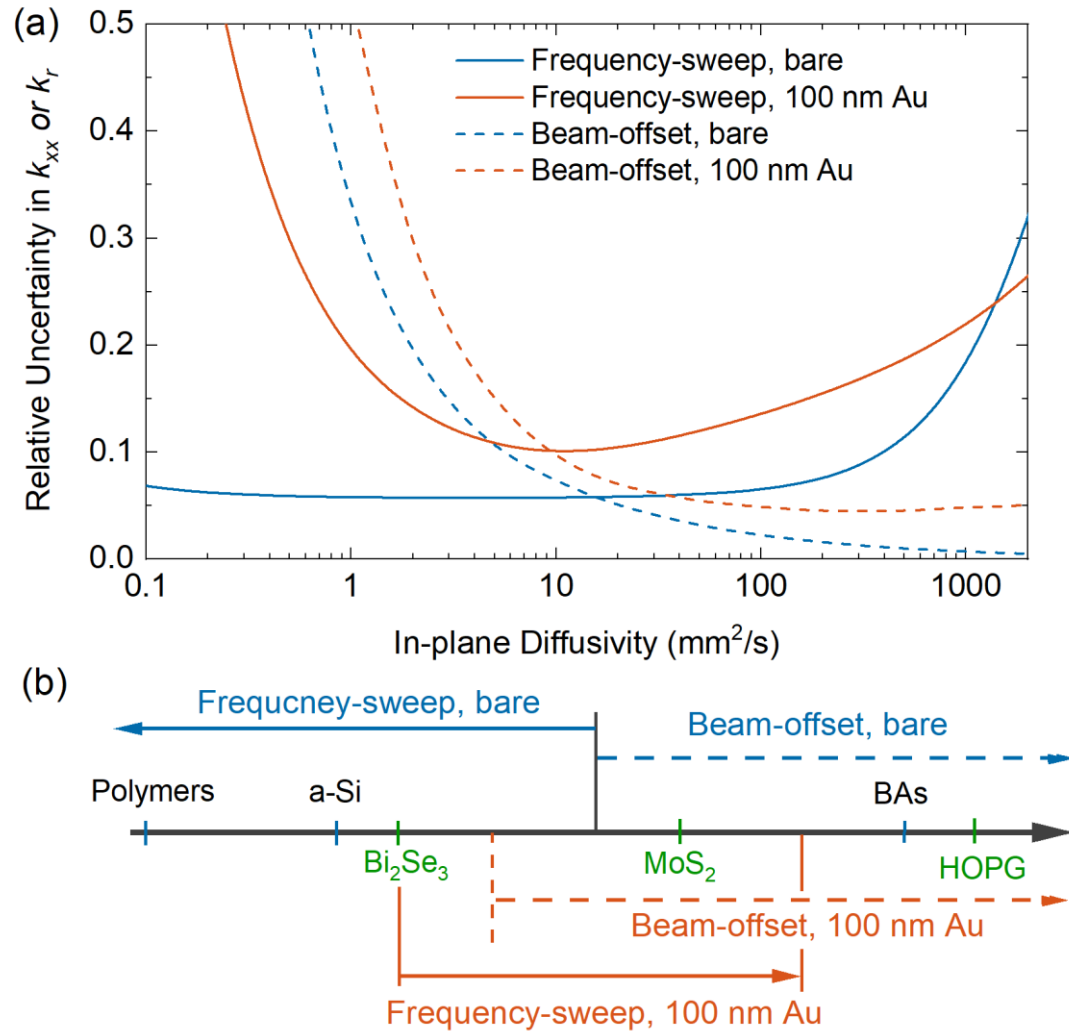


Figure 9. (a) Estimated uncertainty of in-plane thermal conductivity for a wide range of in-plane thermal diffusivities, estimated using a spot radius $w = 3 \mu\text{m}$. (b) Optimal measurement technique for the measurement of in-plane thermal conductivity without transducers (blue arrows) and the optimal range ($<15\%$ uncertainty) with 100 nm Au transducer (red arrows). Thermal conductivity of Au transducer is assumed to be 180 W/mK.

Table II. In-plane thermal conductivity k_r measured by the frequency-sweep FDTR, in-plane thermal conductivity k_{xx} measured by the beam-offset FDTR, and literature values of in-plane thermal conductivity k_r .

Samples	This work		Literature
	k_r by frequency-sweep (W/mK)	k_{xx} by beam-offset (W/mK)	k_r (W/mK)
HOPG	1843 ± 263	1980 ± 165	1900 ± 240 ¹⁹
MoS ₂	75.0 ± 4.1	79.6 ± 4.5	80 ± 14 ¹⁹
Bi ₂ Se ₃	2.75 ± 0.14	2.48 ± 0.32	3.1 ³⁹

Finally, it is helpful to summarize the key points to notice to ensure the validity of transducerless FDTR measurements. The most obvious requirement is that the sample should be absorptive. Before doing the transducerless FDTR measurement, it is always helpful to estimate the light absorption depths δ_0 and δ_1 from the dielectric function or the complex refractive index. One possible scenario the transducerless FDTR might fail, is when measuring materials with the indirect bandgap and long diffusion lengths of photo-excited carriers (much longer than δ_0) like Si, making the heating region deviating from the exponential profile assumed.²⁹ Transducerless FDTR is likely to be valid for direct bandgap semiconductors or metals with fast recombination of photo-excited carriers. The other requirement for transducerless measurement to be valid is the absorption depth of the probe being much smaller than half wavelength in the material $\delta_1 \ll \frac{\lambda_1}{2n}$. However, as already discussed in the appendix, this issue can be mitigated by limiting the measurement below a certain modulation frequency f_{cut} or performing beam-offset

measurement at a fixed frequency below f_{cut} . The cut-off frequency f_{cut} is determined by the condition $d_{pz} = \sqrt{k_z/\pi C f_{cut}} \gg \max\left(\delta_1, \frac{\lambda_1}{2n}\right)$. For a new anisotropic sample with unknown k_r and k_z , it is recommended to perform frequency-sweep and beam-offset measurement for cross-checking. If the in-plane heat diffusivity is higher than 15 mm²/s, transducerless beam-offset measurement alone is able to obtain the in-plane thermal conductivity. For materials with low in-plane thermal diffusivity, only frequency-sweep measurement ensures high sensitivity to k_r . Fortunately, the measurement would still be insensitive to k_z though limiting the highest modulation frequency.

IV. Conclusions

In summary, we proposed a transducerless FDTR method to directly measure in-plane thermal conductivity of nontransparent layered materials. An analytical model including full thermal conductivity tensors and appropriate treatment of light absorption of pump and probe beams is derived. This method not only greatly simplifies the sample preparation in FDTR measurement, but also shows that the sensitivity to in-plane thermal conductivity is greatly improved compared with the conventional FDTR measurement with a transducer film. Through comprehensive sensitivity and error analysis, we show that the in-plane thermal conductivity can be independently determined either by the frequency-sweep FDTR or beam-offset measurement, even when k_{zz} is unknown. This method is experimentally validated using three layered materials with in-plane thermal conductivity which spans over three orders of magnitude: HOPG (~ 1800 W/mK), MoS₂ (~ 80 W/mK) and Bi₂Se₃ (~ 3 W/mK). This work can be easily extended to materials with three-dimensional anisotropy by performing beam-offset measurement along

the different directions, since the thermal model we derived in this work does not assume any crystal symmetry.

Appendix: Limitations of the Thermal Model with Light Absorption

This appendix discusses in more detail the cases when the thermal model with light absorption fails. The first case we consider is silicon with dominant nonradiative recombination and very long lifetime of photo-excited charge carriers on the order of microseconds. Figure 10a indicates that the model shows large discrepancy with the frequency-sweep measurements in the entire modulation frequency range (0.01 MHz to 50 MHz). As we briefly discussed in the maintext, the exponential decaying heating source term in the thermal model is only valid when the diffusion length of charge carriers are smaller than δ_0 and δ_1 . In silicon, the diffusion length of charge carriers can approach $\sim 160 \mu\text{m}$,³⁰ much larger than δ_0 ($\sim 82 \text{ nm}$) and δ_1 ($\sim 0.85 \mu\text{m}$) estimated at 400 nm and 532 nm wavelengths of the pump and probe lasers.⁴⁵ Nonradiative recombination of electron and holes would deposit heat inside the sample in a much wider region compared with the assumed exponentially decaying heating source. Figure 10b also shows that beam-offset measurement also fails to accurately measure thermal conductivity. Thermal conductivity of silicon is overestimated to be $170 \pm 17 \text{ W/mK}$, probably related to the in-plane diffusion of charge carriers that resulted in a larger FWHM of the out-of-phase signal.

The second case we consider is GaAs with dominantly radiative carrier recombination due to its direct bandgap. Although the radiatively recombined light can be reabsorption and recombined, the heating created by this part of the energy should be more or less uniformly distributed in the entire sample which does not affect temperature distribution. The above-

bandgap heating source profile can still be approximated by e^{-z/δ_0} . However, we still found that the thermal model failed to fit the frequency-sweep signal in the high frequency range (> 1.0 MHz) as shown in Figure 10c. Such discrepancy can be attributed to the relative long absorption depth of the probe beam δ_1 (estimated to be ~ 111 nm)³², which is comparable with the half-wavelength $\lambda_1/2n = 136$ nm inside the media, where λ_1 is the probe wavelength (532 nm) and n is real part of the refractive index.³² In this case, the phase delay of the internally reflected beam is nonnegligible, and Eq. (7) no longer holds.^{25, 29} However, this problem can be partially resolved by fitting the data only at low modulation frequency. In the low frequency range, thermal penetration depth d_{pz} ranging from 4 μm at 1.0 MHz to 28 μm at 0.01 MHz is much larger than both δ_1 and $\lambda_1/2n$. This scenario can be approximated as surface probing and the thermal model would become less sensitive to the exact profile of the probe intensity. Indeed fitting the frequency-sweep signal below 0.5 MHz shown in Figure 10c can still achieve reasonable fitting and we extract the thermal conductivity of GaAs to be 48.0 ± 8.5 W/mK. In Figure 10d, the thermal conductivity of GaAs is also measured to be 43.2 ± 2.4 W/mK with beam-offset measurement at 0.14 MHz and in good agreement with the frequency-sweep measurement and the literature value (52 W/mK).⁴⁶

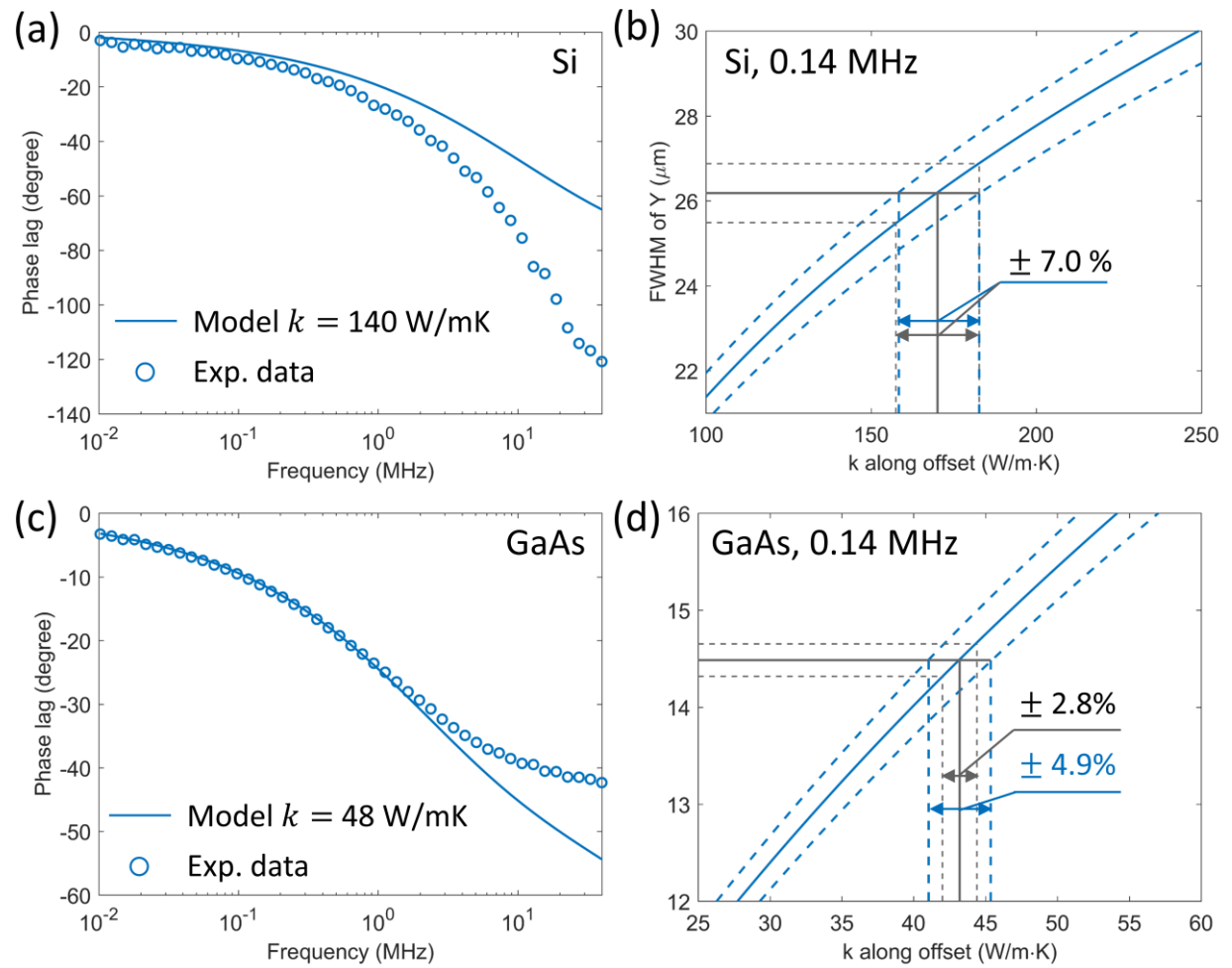


Figure 10. (a) Frequency-sweep measurement of bare Si without transducer. (b) Beam-offset measurement result of bare Si without transducer. Gray dashed line indicates the experimental uncertainty contribution from the FWHM measured at $f = 0.14$ MHz, and the blue dashed line indicates the uncertainty contribution from the simulated FWHM as a function of k_{xx} . Both contributed $\sim 7\%$ of the error in final thermal conductivity result. The final beam-offset result is 170 ± 17 W/mK, which overestimated the thermal conductivity of silicon. (c) Frequency-sweep measurement of bare GaAs without transducer. (d) Beam-offset measurement result of bare GaAs without transducer. Final result obtained is 43.2 ± 2.4 W/mK.

Acknowledgement: The authors acknowledge funding support by Grant No. W911NF-19-1-0279 and NSF CBET-1851052. X. Q. acknowledges helpful discussions with Yoichiro Tsurimaki and Xinpeng Zhao. The authors declare no conflict of interest.

References:

1. L. D. Zhao, S. H. Lo, Y. Zhang, H. Sun, G. Tan, C. Uher, C. Wolverton, V. P. Dravid and M. G. Kanatzidis, *Nature* **508** (7496), 373-377 (2014).
2. O. Hellman and D. A. Broido, *Phys. Rev. B* **90** (13) (2014).
3. M. Higashiwaki, K. Sasaki, T. Kamimura, M. Hoi Wong, D. Krishnamurthy, A. Kuramata, T. Masui and S. Yamakoshi, *Appl. Phys. Lett.* **103** (12), 123511 (2013).
4. W. S. Hwang, A. Verma, H. Peelaers, V. Protasenko, S. Rouvimov, H. Xing, A. Seabaugh, W. Haensch, C. V. de Walle, Z. Galazka, M. Albrecht, R. Fornari and D. Jena, *Appl. Phys. Lett.* **104** (20), 203111 (2014).
5. X. Qian, P. Jiang and R. Yang, *Materials Today Physics* **3**, 70-75 (2017).
6. J. O. Besenhard, *Carbon* **14** (2), 111-115 (1976).
7. J. O. Besenhard and H. P. Fritz, *Electroanalytical Chemistry and Interfacial Electrochemistry* **53**, 329-333 (1974).
8. K. Chang and W. Chen, *ACS Nano* **5** (6), 4720-4728 (2011).
9. L. David, R. Bhandavat and G. Singh, *ACS Nano* **8** (2), 1759-1770 (2014).
10. Z. X. Shu, R. S. McMillan and J. J. Murray, *J. Electrochem. Soc.* **140** (4), 992 (1993).
11. X. Qian, X. Gu, M. S. Dresselhaus and R. Yang, *J Phys Chem Lett* **7** (22), 4744-4750 (2016).
12. D. G. Cahill, *Rev. Sci. Instrum.* **75** (12), 5119-5122 (2004).
13. A. J. Schmidt, *Annual Review of Heat Transfer* **16** (1), 159 (2013).
14. A. J. Schmidt, R. Cheaito and M. Chiesa, *Rev. Sci. Instrum.* **80** (9), 094901 (2009).
15. K. T. Regner, S. Majumdar and J. A. Malen, *Rev. Sci. Instrum.* **84** (6), 064901 (2013).
16. J. Zhu, D. Tang, W. Wang, J. Liu, K. W. Holub and R. Yang, *J. Appl. Phys.* **108** (9), 094315 (2010).
17. A. J. Schmidt, X. Chen and G. Chen, *Rev. Sci. Instrum.* **79** (11), 114902 (2008).
18. P. Jiang, X. Qian, X. Gu and R. Yang, *Adv. Mater.* **29**, 1701068 (2017).
19. P. Jiang, X. Qian and R. Yang, *Rev. Sci. Instrum.* **88** (7), 074901 (2017).
20. J. P. Feser, J. Liu and D. G. Cahill, *Rev. Sci. Instrum.* **85** (10), 104903 (2014).
21. P. Jiang, X. Qian and R. Yang, *Rev. Sci. Instrum.* **89** (9), 094902 (2018).
22. M. Li, J. S. Kang and Y. Hu, *Rev. Sci. Instrum.* **89** (8), 084901 (2018).
23. P. Jiang, X. Qian and R. Yang, *J. Appl. Phys.* **124** (16), 161103 (2018).
24. J. Liu, G.-M. Choi and D. G. Cahill, *J. Appl. Phys.* **116** (23), 233107 (2014).
25. J. Yang, E. Ziade and A. J. Schmidt, *J. Appl. Phys.* **119**, 095107 (2016).

This is the author's peer reviewed, accepted manuscript. However, the online version of record will be different from this version once it has been copyedited and typeset.
PLEASE CITE THIS ARTICLE AS DOI:10.1063/1.50003770

26. L. Wang, R. Cheaito, J. L. Braun, A. Giri and P. E. Hopkins, *Rev. Sci. Instrum.* **87** (9), 094902 (2016).
27. J. M. Powers, *J. Heat Transfer* **126**, 670-675 (2004).
28. G. Chen, *Nanoscale energy transport and conversion*. (Oxford University Press, ISBN: 9780195159424, 2005).
29. G. Chen, *Annual Review of Heat Transfer* **7**, 1-57 (1996).
30. J. Batista, A. Mandelis and D. Shaughnessy, *Appl. Phys. Lett.* **82** (23), 4077-4079 (2003).
31. C. Thomsen, H. T. Grahn, H. J. Maris and J. Tauc, *Phys Rev B Condens Matter* **34** (6), 4129-4138 (1986).
32. A. D. Rakić and M. L. Majewski, *J. Appl. Phys.* **80** (10), 5909-5914 (1996).
33. R. B. Wilson, J. P. Feser, G. T. Hohensee and D. G. Cahill, *Phys. Rev. B* **88** (14), 144305 (2013).
34. D. M. Hamby, *Environ. Monit. Assess.* **32**, 135-154 (1994).
35. W. DeSorbo and W. W. Tyler, *J. Chem. Phys.* **21**, 1660 (1953).
36. G. E. Jellison, J. D. Hunn and H. N. Lee, *Phys. Rev. B* **76** (8) (2007).
37. L. S. Volovik, V. V. Fesenko, A. S. Bolgar, S. V. Drozdova, L. A. Klochkov and V. F. Primachenko, *Soviet Powder Metallurgy and Metal Ceramics* **17**, 697-702 (1978).
38. M. S. Ullah, A. H. B. Yousuf, A. D. EsSakhi and M. H. Chowdhury, *AIP Conf. Proc.*, 020001 (218).
39. J. Navrátil, J. Horák, T. Plecháček, S. Kamba, P. Lošťák, J. S. Dyck, W. Chen and C. Uher, *J. Solid State Chem.* **177** (4-5), 1704-1712 (2004).
40. D. Fournier, M. Marangolo, M. Eddrief, N. N. Kolesnikov and C. Fretigny, *J. Phys.: Condens. Matter* **30** (11), 115701 (2018).
41. J. Humlíček, D. Hemzal, A. Dubroka, O. Caha, H. Steiner, G. Bauer and G. Springholz, *Phys. Scr.* **T162**, 014007 (2014).
42. J. Yang, E. Ziade and A. J. Schmidt, *Rev. Sci. Instrum.* **87** (1), 014901 (2016).
43. X. Qian, P. Jiang, P. Yu, X. Gu, Z. Liu and R. Yang, *Appl. Phys. Lett.* **112** (24), 241901 (2018).
44. J. Yang, C. Maragliano and A. J. Schmidt, *Rev. Sci. Instrum.* **84** (10), 104904 (2013).
45. D. E. Aspnes and A. A. Studna, *Phys. Rev. B* **27** (2), 985-1009 (1983).
46. Y. K. Koh and D. G. Cahill, *Phys. Rev. B* **76** (7), 075207 (2007).

